

Article

# A Basic Complete Numerical Toolbox for Picosecond Ultrasonics

**Philippe Babilotte**

Spectrum Engineering Department, French National Frequency Agency, ANFR/DPSAI/IS, CS 13829, 29238 Brest CEDEX 03, France; philippe.babilotte@anfr.fr or philip.babilotte@laposte.net

Received: 27 November 2018; Accepted: 13 January 2019; Published: 17 January 2019



**Abstract:** A complete numerical complete toolbox is proposed concerning the simulation of photo-induced propagative mechanical wave, and concerning the optical reflectometric measured response of the material, which is initially exposed to a first pump laser beam that photo-induces the acoustic wavefronts. The deformation field and its propagation into a bulk material are simulated. Based on this field expression, the complex transient reflectivity is given for a medium considered as homogeneous. The real part of this quantity permits afterwards to propose a numerical simulation of the transient reflectivity, which corresponds to the optical signal measured during experimental works. The frequency acoustic spectrum is simulated and successfully compared to the measured frequency spectrum. For the first time, numerical complete developments are explicitly proposed and fully-developed under the *SciLab*<sup>®</sup> environment, related to the simulation of laser-induced picosecond acoustic wavefront photogenerated through an opto-acoustic transduction process (ultrasonics and pretersonics).

**Keywords:** simulation; computational acoustics; laser ultrasonics; optical reflectivity; acoustic waves; pretersonics

**PACS:** 62.20.F-; 43.35.Sx; 78.20.hb; 42.15.Dp

## 1. Presentation of the General Concept

Ultra-high frequency coherent acoustic phonons can be photogenerated and photodetected using a pump–probe laser scheme [1–3]. High frequency acoustic waves into the *GHz* or into the sub-*THz* frequency domain can be optically excited and detected by femtoseconde (*fs*) laser pulses [4]. Conventional (piezo-electric) transducers approach or photo-acoustic transduction approach involving a metal layer absorbing a nanoseconde (*ns*) laser pump pulse [5] are unable to reach such ultra-high frequency content [6]. The ultrasonic approach becomes, therefore, the only relevant way to generate and to detect such high frequency ranges. Schematically, a transient mechanical strain pulse is photogenerated into the bulk of the material, after interaction of the first pump laser pulse with the matter, through an opto-acoustic transduction (Figure 1). These photo-induced coherent phonons (propagative elastic disturbance) can be afterwards detected using a second laser light temporally synchronized and delayed-in-time to the first pump pulse [4]. The photodetection is based onto an acousto-optic transduction, revealing the propagation of the acoustic signal. Acoustical waves (laser-induced transient stress) can be, therefore, generated using ultrashort optical pulses [1,7]. The detection process [4,7–11] corresponds to a time domain optical spectroscopy [1,2,4,7,8,12–14]. The time-resolved optical pump–probe experimental set-up involved is given in Figure 2.

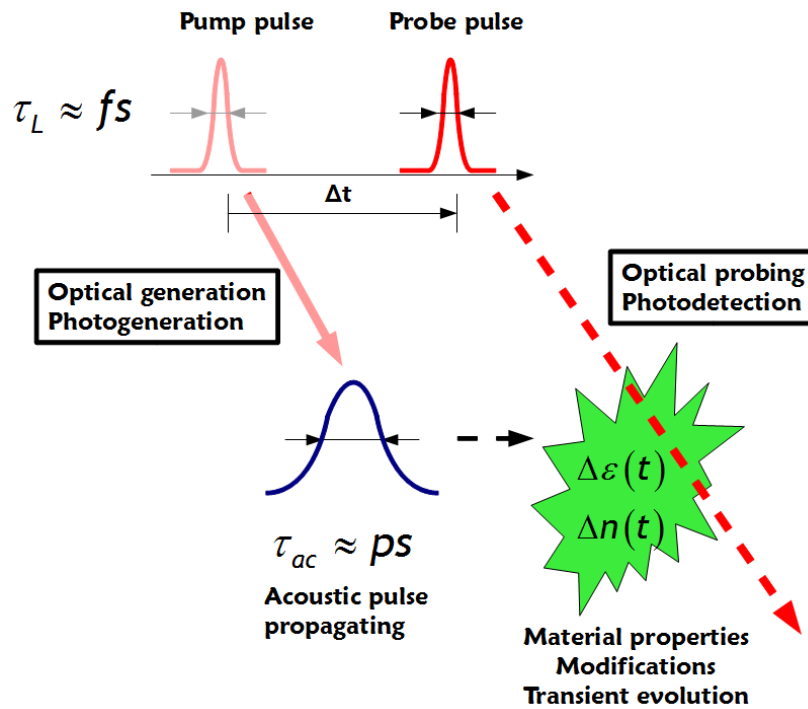


**Figure 1.** Laser picosecond ultrasonics.  $\tau_L$  corresponds to a femtoseconde ( $fs$ ) laser pulse duration (pump and probe laser pulse).  $\tau_{ac}$  corresponds to the picosecond acoustic signal ( $ps$ ). Opto-acoustic transduction (optical absorption and energy transfer process). The propagative acoustic signal induces  $\Delta \epsilon$  and  $\Delta n$ . Optical probing using a pump–probe set-up (temporal delay to monitor the transient  $\partial_t \Delta \epsilon(t)$  and  $\partial_t \Delta n(t)$  variations, induced by the acoustic wave.

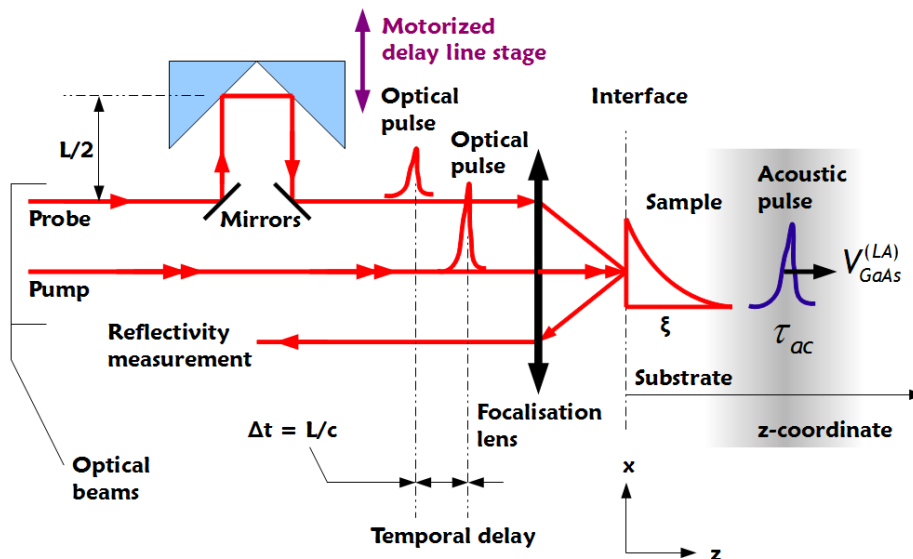


**Figure 2.** Typical all-optical time-resolved pump–probe set-up involved for reflectometry measurements. In-depth coordinate  $z$ .  $L$  corresponds to the additional optical pathway ( $\Delta t$  delay time) due to the presence of the delay line stage (probe beam).  $\xi$  is the optical depth penetration.  $(O, \vec{x}, \vec{z})$  is a symmetry plan as the spot size is  $\Phi \gg \xi$ . Acoustic pulse duration  $\tau_{ac}$  (photo-excited propagative wavefront). Acoustic velocity  $V_{GaAs}^{(LA)}$  according to the LA mode.

From these optical reflectivity measurements [8], key quantities can be extracted such as thickness, sound velocity, attenuation coefficient, refractive index, elastic, optical, thermophysical and mechanical properties [4,15] of submicrometric and nanometric size substrates, nano-multilayers, or bulk materials [10] and even liquids [16]. Longitudinal acoustic (LA) propagative acoustic waves can be detected, for instance, in liquid water, monitoring backscattered probe light from the sound wave propagating into the liquid [17], and, therefore, providing information about the medium itself. This opto-acoustic approach has then been found relevant for material characterization [18] and non-destructive evaluation (NDE) of mechanical or elastic properties of thin film [19,20], for mechanical strength determination of industrial materials (such as silicon wafers) [21,22] or non-destructive testing of materials (NDT) such as graphite fibers re-inforced composites for instance [23,24], for detection of residual stress into metal [6,25], for non-invasive photo-acoustic diagnostics of biological tissues [26], for photo-acoustic gas spectroscopy [27,28], for interface defect detection [18,29], for breaking cracks, voids, faults, flaws, or surface and sub-surface defects into semi-conductors [30–32], for bubbles or volumic defects [33], considering the modification of the photo-elastic response if local defects are present into the material [5]. This ultrasonic (also called picosecond laser acoustics) proposes then a versatile, precise and contact-free analytic tool for material sciences or industrial process control [4,34].

If extensive research activities and fundamental or engineering aspects have been extensively studied, no particular works proposed developments around numerical simulations and coding of reflectometric signal simulations, wavefronts simulations, and ultrasonics. Simulations of several experimental quantities are, therefore, proposed into the present work, considering the absence of any shockwaves [35], nor ablation or any destructive processes, and considering a linear absorption of the photogeneration laser beam at the interface (modelization out of any special conditions).

A complete numerical study is then presented, for the first time, given under the *SciLab*<sup>®</sup> environment, based on a commonly accepted experimental set-up, described in Figure 2. A complete numerical study is proposed under a basic approach. The optical absorption parameter  $\alpha$ , the optical depth penetration  $\xi$ , and the elastic stiffness  $C$  will be first numerically introduced, as primary inputs into the codes. Acoustics velocities will be afterwards directly estimated. Brillouin frequencies will be calculated next, estimating the impact of the incidence angle  $\theta$  of the laser probe beam and the impact of the medium temperature  $T$ . The deformation field and its dynamic evolution can be then evaluated. Based onto these elements and primary parameters, the transient reflectivity is numerically and entirely simulated, and compared to original experimental measured data, obtained using the optical set-up described. All the given simulation codes given provide a complete numerical toolbox for laser ultrasonics works, as the proposed codes could next be also implemented according to users' wishes.

## 2. Numerical Study

In the present work, for all the proposed simulations, a red probe and a red laser pump are considered (Figure 2), as this basic configuration is commonly used in experimental works [8].

A *GaAs* (100) substrate is considered, as this semi-conductor can be seen as a condensed matter model in fundamental physics. No particular nitridation of the substrate surface [36], nor particular presence of *AsAs* adsorbed ad-atoms dimers, nor *GaGa* dimers presence [37], nor  $\text{As}_2\text{O}_3$  or  $\text{Ga}_2\text{O}_3$  oxidised islands [38] are considered for all the numerical developments proposed in this work. As an extension, all the proposed codes could be re-used for another medium, changing the relevant parameters.

### 2.1. Optical Absorption Coefficient and Optical Depth Penetration

Two expressions  $\alpha^{(s)}$  and  $\alpha^{(p)}$  are then introduced, for pump (( $p$ ) index) and probe beam (( $s$ ) index), concerning the optical absorption coefficient:

$$\alpha^{(s,p)} = \frac{4\pi}{\lambda^{(s)}} \times \Im m \left( n_{GaAs}^{(s,p)} \right) \quad (1)$$

in which  $\lambda^{(s)}$  corresponds to the optical probe wavelength, and if  $n_{GaAs}^{(s,p)}(\lambda^{(s)})$  corresponds to the reference index of *GaAs* at the probe wavelength  $\lambda^{(s)}$ . For the proposed work,  $n_{GaAs}^{(s,p)}(\lambda^{(s)} = 800.8 \text{ nm}) = 3.66 + 0.08i$  is used [39]. In the present study, a red-red (800.8 nm or 1.55 eV exact energy value) pump–probe configuration is used, and it comes  $\alpha^{(s)} = \alpha^{(p)} \equiv \alpha^{(s,p)}$ .

Into the picosecond ultrasonic experiments, the first optical pulse (pump beam) is typically absorbed at the free surface of the substrate interface under the absorption length  $\delta$ , corresponding, in first approximation, *without any supersonic diffusion of carriers* [40], to the optical depth penetration  $\zeta$ . As both pump beam and probe beam are used into the red wavelength, we have:

$$\delta^{(s,p)} \equiv \zeta^{(s,p)} = \frac{1}{\alpha^{(s,p)}} \quad (2)$$

Calculations concerning the  $\zeta$  evaluation gives nevertheless strong differences according to the wavelength values involved [39,41]. For instance, the optical depth penetrations are, therefore, numerically estimated at  $\approx 15 \text{ nm}$  for 400.4 nm irradiation, and estimated at  $\approx 400 \text{ nm}$  for 800.8 nm laser irradiation ( $\approx 26$  times higher value).

```
//Scilab code (part 01/13)
clear all //Clear
clc() //Clear

lambdap = 800.8 * 10^(-9) //Probe optical wavelength (m)
lambdas = 800.8 * 10^(-9) //Pump optical wavelength (m)

n0 = 1.0002772 //Air around the sample (refractive index)
k0 = (2*%pi*n0)/lambdas //Evaluation of the wavevector for optical wave
Z0 = 0.0429 * 10^(4) //Acoustic impedance of the air (kg.m-2.s-1)

//Density of the medium (kg.m-3)
rhoGaAs = 5317 //5.320 g.cm-3 (reference value)

//Angle value close to zero (normal incidence for pump beam)
//thetaDeg = 0
thetaDeg = 45 //for probe
theta = thetaDeg * (%pi/180) //Angle (from degrees to radians)
```

```
//Scilab code (part 02/13)
//GaAs bulk parameters (taken at 1.55 eV exact value)
//Refraction index values at the wavelength (nm) for GaAs
n2p = 3.66+%i*0.08 //1.55 eV (800.8 nm)
n2s = 3.66+%i*0.08 //1.55 eV (800.8 nm)
nGaAs=real(n2s)

//Optical absorption coefficient (pump and probe)
alphas=4*%pi*imag(n2s)/lambdas
alphap=4*%pi*imag(n2p)/lambdas

//Optical depth penetration for probe and pump
xis=1/(alphas)
xip=1/(alphap)

//Ratio between optical depth penetration (test, should be equal to 1)
ratioxi=xip/xis
```

## 2.2. Acoustic Velocities Calculations

The different values of the acoustic velocities can be estimated from the stiffness matrix coefficient  $C_{mn}$  ( $m, n$  index), the anisotropy factor  $A$  and the density  $\rho$ . For this purpose, *Burenkov* relationship, involving  $C_{11}$ ,  $C_{12}$  and  $C_{44}$  [42], under the melting point temperature (around 1510–1515 K [42]), are used:

$$\begin{cases} C_{11}(T) = (12.17 - 1.44 \times 10^{-3} \times T) \times 10^{-1} \times 10^{11} \\ C_{12}(T) = (5.46 - 0.64 \times 10^{-3} \times T) \times 10^{-1} \times 10^{11} \\ C_{44}(T) = (6.16 - 0.70 \times 10^{-3} \times T) \times 10^{-1} \times 10^{11} \end{cases} \quad (3)$$

```
//Scilab code (part 03/13)
T = 298.15 //Temperature considered (K), room temperature (RT) condition

//Stiffness matrix coefficient values
//Units: dyn/cm2 divided by 10 \textcolor{black}{corresponds to} N/m2
c11= ((12.17-1.44*T*1e-3)/10)*1e11 //Elastic rigidity (N/m^2)
c12= ((5.46 - 0.64*T*1e-3)/10)*1e11 //Elastic rigidity (N/m^2)
c44= ((6.16 - 0.70*T*1e-3)/10)*1e11 //Elastic rigidity (N/m^2)
```

The pure longitudinal acoustic (*resp.* transverse acoustic) modes LA (*resp.* TA) is given by:

$$V_{GaAs}^{LA} = \left( \frac{C_{11}}{\rho} \right)^{1/2} \quad (4)$$

$$V_{GaAs}^{TA} = \left( \frac{C_{44}}{\rho} \right)^{1/2} \quad (5)$$

The quasi-longitudinal (*resp.* quasi-transverse) acoustic modes QLA (*resp.* QTA) is given by:

$$V_{GaAs}^{QLA} = \left( \frac{C_{11} + C_{44} \times \left(1 - \frac{1}{A}\right)}{\rho} \right)^{1/2} \quad (6)$$

$$V_{GaAs}^{QTA} = \left( \frac{C_{44}}{\rho A} \right)^{1/2} \quad (7)$$

introducing the *Zener* anisotropy factor  $A$ :

$$A = \frac{2C_{44}}{C_{11} - C_{12}} \quad (8)$$

Few numerical results are given in Table 1, concerning the calculated acoustic velocities and the related Brillouin frequencies.

A *GaAs* (100) substrate is considered for all the simulations, and [100] corresponds to a propagation direction for the LA mode (involving the coefficient  $C_{11}$ ), coupled to the two transverse modes TA1 and TA2 ( $C_{44}$ ).

```
//Scilab code (part 04/13)
//Anisotropy factor (adimensional factor)
A=(2*c44)/(c11-c12)

//Pure longitudinal wave [100] direction
VLGaAsEstim=(c11/rhoGaAs)^0.5

//Pure shear wave [010] polarized
VTAGaAsEstim=(c44/rhoGaAs)^0.5

//Quasi-longitudinal wave
VQLAGaAsEstim=((c11+(c44*(1-(1/A))))/rhoGaAs)^0.5

//Quasi-shear wave
VQTAGaAsEstim=(c44/(A*rhoGaAs))^0.5

//Acoustic impedance for GaAs bulk material (kg.m-2.s-1)
ZGaAs = rhoGaAs * VLAGaAsEstim

//Evaluation of difference of impedance values (kg.m-2.s-1)
\textcolor{black}{//Test}
DeltaZ = ZGaAs-Z0 \textcolor{black}{
{//Z0 impedance of the air (reference level)}
Diff=DeltaZ/ZGaAs*100 \textcolor{black}{
{//Strong or low interface}}
```

Considering a typical optical depth penetration  $\xi$ , and the LA (longitudinal acoustic) sound velocity  $V_{GaAs}^{(LA)}$ , the expected duration  $\tau_{ac}$  of the acoustic pulses is given by:

$$\tau_{ac} \equiv \frac{\xi}{V_{GaAs}^{(LA)}} \quad (9)$$

The characteristic frequency  $f_{ac}$  of these acoustic waves can be afterwards deduced:

$$f_{ac} \equiv (2\pi\tau_{ac})^{-1} \tag{10}$$

$Z_{GaAs} = \rho_{GaAs}V_{GaAs}^{(LA)}$  corresponds to the acoustic impedance of the substrate for LA mode of propagation.

### 2.3. Brillouin Frequencies Calculations

The Brillouin frequencies  $f_{GaAs}^{(m)}$ , considering the different modes  $m = \{LA, TA, QLA, QTA\}$ , results from an interference phenomenon between the two beam coming from the incoming probe itself, as described in Figure 3 [43,44]:

$$f_{GaAs}^{(m)} = \frac{2V_{GaAs}^{(m)}}{\lambda^{(s)}} \times \left( n_{GaAs}^{(s)2} - n_0^2 \sin^2 \theta \right)^{1/2} \tag{11}$$

in which  $\lambda^{(s)}$  corresponds to the optical probe wavelength [9], and  $\theta$  to the angle related to the normal incidence (above the sample surface), considering the different modes  $m$  and the index of refraction  $n_{GaAs}^{(s)}$  of *GaAs* at the wavelength  $\lambda^{(s)}$  of the optical probe [14,39,44]. Numerical results are then given in Table 1 for an angle  $\theta = 45^\circ$  for the probe beam incidence, corresponding also to a typical angular value (experimental data). For instance, a  $\Delta\theta \approx 10^\circ$  variation of incidence angle (centered onto  $45^\circ$  value), induces roughly a  $\Delta f_{GaAs}^{(m)} \approx 0.3$  ps variation for the Brillouin period, as given into the numerical results (Figure 4).

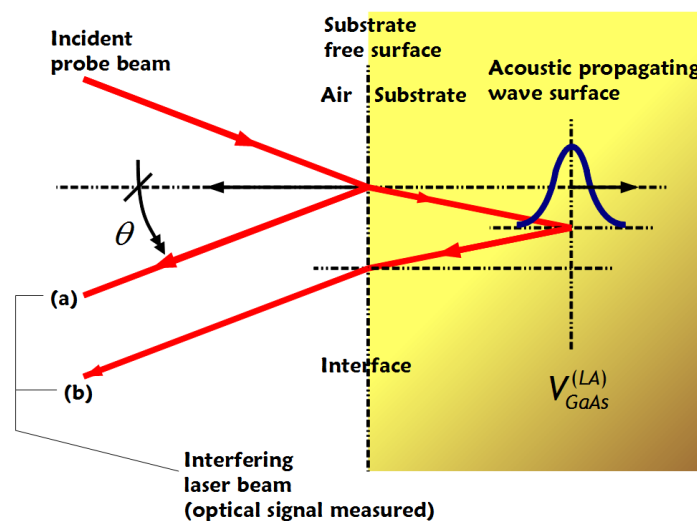


**Figure 3.** Brillouin oscillation interference (probe beam) between the incident beam directly reflected onto free surface (a) and the incoming beam reflecting onto the in-depth propagative waveplane (b). Longitudinal velocity of the propagative acoustic wave  $V_{GaAs}^{(LA)}$ . Angle of incidence  $\theta$  for probe beam.

```

//Scilab code (part 05/13)
//Brillouin frequency mode value (Hz) for LA mode
fBLA=((2*VLGaAsEstim)/lambdas)*((nGaAs*nGaAs)-(sin(theta))^2)^(0.5)
fBLA_GHz = fBLA * 10^(-9)

//Brillouin frequency mode value (Hz) for TA mode
fBTA=((2*VTAGaAsEstim)/lambdas)*((nGaAs*nGaAs)-(sin(theta))^2)^(0.5)
fBTA_GHz = fBTA * 10^(-9)

//Brillouin frequency mode value (Hz) for QLA mode
fBQLA=((2*VQLGaAsEstim)/lambdas)*((nGaAs*nGaAs)-(sin(theta))^2)^(0.5)
fBQLA_GHz = fBQLA * 10^(-9)

//Brillouin frequency mode value (Hz) for QTA mode
fBQTA=((2*VQTAGaAsEstim)/lambdas)*((nGaAs*nGaAs)-(sin(theta))^2)^(0.5)
fBQTA_GHz = fBQTA * 10^(-9)

```

The impact on the Brillouin value  $f_{GaAs}^{(m)}$  of the two physical parameters (angle of incidence  $\theta$  and temperature  $T$ ) has been simulated in Figures 4 and 5, as  $C_{11}$ ,  $C_{12}$  and  $C_{44}$  are temperature dependent [42]. These parameters variations can have, therefore, a significant impact onto the Brillouin frequency value.

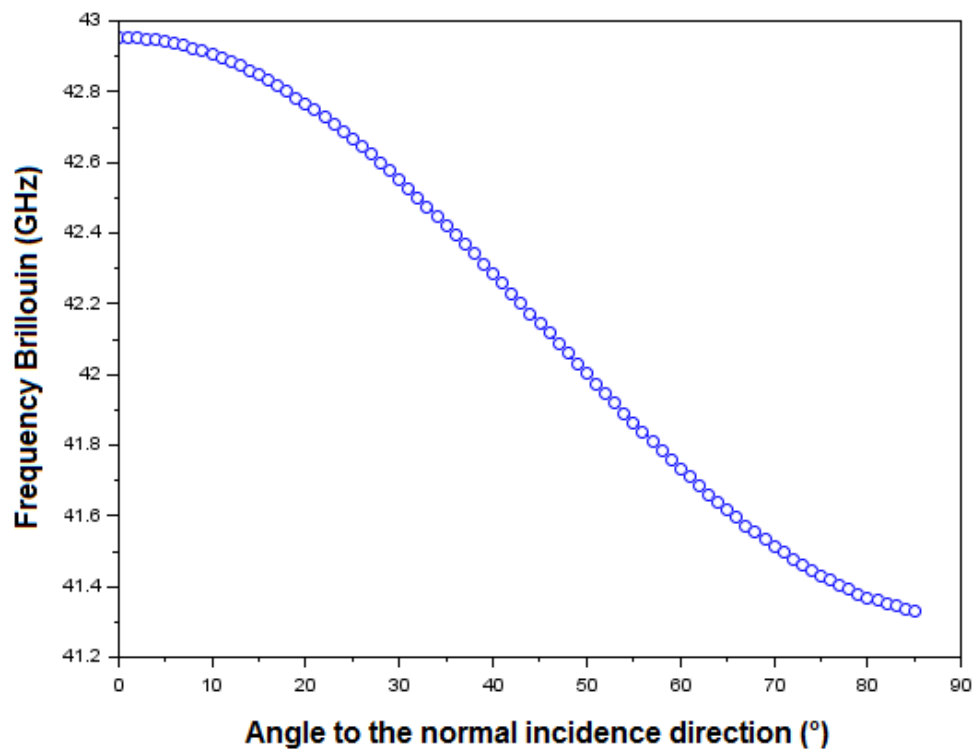


**Figure 4.** Numerical evaluation of the impact of the incidence angle  $\theta$  (for probe beam) onto the Brillouin frequency value  $f_{GaAs}^{(LA)}$  (standard temperature fixed at 298.15 K), for GaAs.

```
//Scilab code (part 06/13)
VLGAAsEstim=(c11/rhoGaAs)^0.5
fBLA=((2*VLGAAsEstim)/lambdas)*((nGaAs*nGaAs)-(sin(theta))^2)^(0.5)
//Brillouin frequency mode value (Hz) for LA mode
fBLA_GHz = fBLA * 1e-9

scf(0)
clf(0)
T=0:5:1400;
plot(T,fBLA_GHz,'-o');
xlabel('Temperature (K)')
ylabel('Brillouin frequency (GHz)')
title('Impact of the temperature onto the Brillouin frequency,
for 45 angle incidence to normal direction.')
```

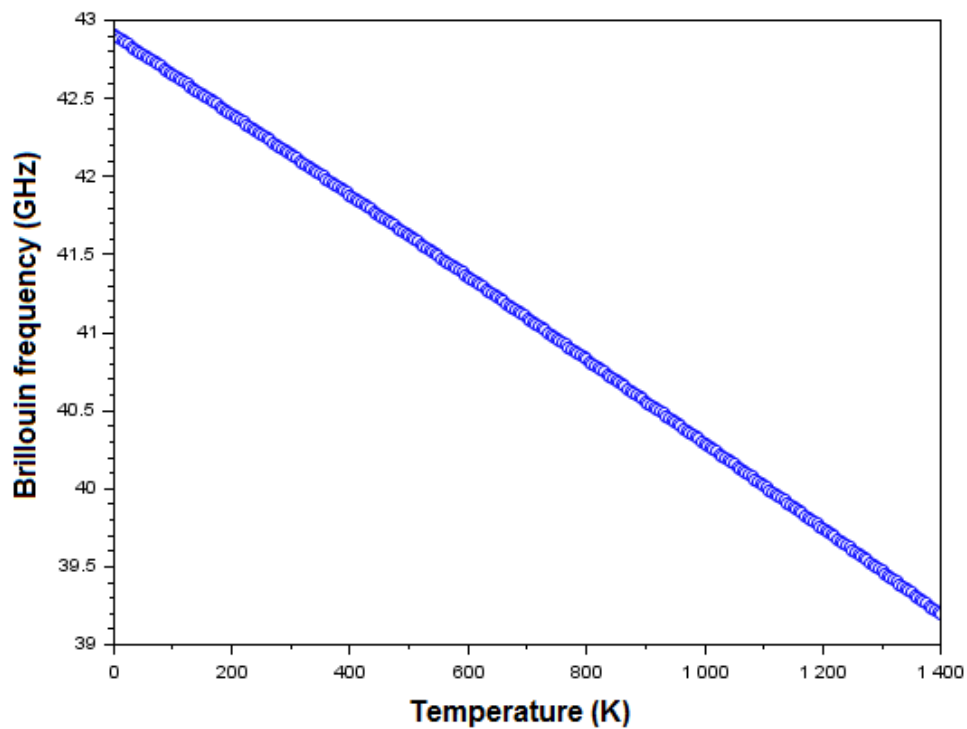


**Figure 5.** Numerical evaluation of the impact of the temperature  $T$  onto the Brillouin frequency value (under the melting temperature), for  $GaAs$ , for a typical angle of incidence to perpendicular direction numerically fixed at  $45^\circ$  (probe beam), for  $LA$  mode.

**Table 1.** Numerical calculations of acoustic velocities and Brillouin frequency (temperature fixed at 298.15 K and angle of incidence fixed at  $45^\circ$ ).

Velocity	( $m \cdot s^{-1}$ )	Brillouin Frequency	(GHz)
$V_{GaAs}^{(LA)}$	4725.6	$f_{GaAs}^{(LA)}$	42.4242
$V_{GaAs}^{(TA)}$	3341.5	$f_{GaAs}^{(TA)}$	29.9984
$V_{GaAs}^{(QLA)}$	5233.3	$f_{GaAs}^{(QLA)}$	46.9824
$V_{GaAs}^{(QTA)}$	2231.5	$f_{GaAs}^{(QTA)}$	22.1895

```

//Scilab code (part 07/13)
clear all //Clear
clc() //Clear
T = 298.15 //25 degrees, temperature of the medium
//Elastic coefficient for GaAs (elastic rigidity expressed in N/m^2)
c11= ((12.17-1.44*T*1e-3)/10)*1e11
c12= ((5.46 - 0.64*T*1e-3)/10)*1e11
c44= ((6.16 - 0.70*T*1e-3)/10)*1e11
A=(2*c44)/(c11-c12)
rhoGaAs = 5317

thetaDeg=0:2:80;
theta = thetaDeg * (%pi/180)
VLGAAsEstim=(c11/rhoGaAs)^0.5
fBLA=((2*VLGAAsEstim)/lambdas)*((nGaAs*nGaAs)-(sin(theta))^2)^(0.5)
fBLA_GHz = fBLA * 1e-9
scf(0)
clf(0)
thetaDeg=0:2:80;
plot(thetaDeg,fBLA_GHz,'-o');
xlabel('Incidence angle (degree)')
ylabel('Brillouin frequency (GHz)')
title('Impact of the angle incidence value onto the Brillouin frequency,
for 298.15 K temperature.')

```

#### 2.4. Deformation Field Simulation

The optical wave (pump) is supposed to be absorbed beneath the interface, and the acoustic wave (optically generated acoustic "disturbance") is propagating into the bulk, from  $z = 0$  to  $+\infty$  (in-depth coordinate). The probe pulse is supposed to be deflected onto the  $z = 0$  interface and also onto the in-depth acoustic waveplan propagating at the velocity  $V_{GaAs}^{(LA)}$ , inducing, therefore, typical Brillouin interference pattern (according to the Figure 3 configuration). No particular echo should be detected without any present particular bulk defects. Unidimensional configuration is considered, as  $\Phi \gg \xi$  (typically  $\Phi \approx 10 \mu\text{m}$  for the optical beam spot size used into typical ultrasonic experiments). A longitudinal acoustical mode  $LA$  is consequently supposed to be excited into the matter.

#### 2.5. Deformation Field

The deformation field [45] and the propagative acoustic wave present into the bulk material are modeled involving a standard *Heaviside*  $\mathcal{H}$  step function, for spatial  $z$  and time  $t$  variables. Introducing  $\varphi(z, t) = z - V_{GaAs}^{(LA)}t$ , the total field  $\eta(z, t)$  used for the simulation is given by:

$$\eta(z, t) = \left(2 - e^{-\alpha^{(p)}V_{GaAs}^{(LA)}t}\right) \times e^{-\alpha^{(p)}z} \times \mathcal{H}(z) - e^{-\alpha^{(p)}|\varphi(z,t)|} \times \mathcal{H}(\varphi(z, t)) \quad (12)$$

```
//Scilab code (part 08/13)
//Heaviside step function H(z) definition
deff('y=H(x)', 'if x<0 then y=0;else y=1;end;')

function[Sci]=defo(alphap,t,z)
defs3=
(2-exp(-alphap.*VLAGaAsEstim.*t))*exp(-alphap*z)*H(z)-
H(z-VLAGaAsEstim*t)*exp(-alphap*abs(z-VLAGaAsEstim*t));
def=1.5*defs3; //Arbitrary scale factor
Sci=def';
endfunction
```

The temporal evolution of the deformation field (*LA* mode) can be, therefore, proposed, simulating the wavefront propagation into the substrate (Figure 6). Similar results can be obtained using the *erf* function instead an *Heaviside* step-function.

The value of the geometrical parameter  $\delta \equiv \zeta$  can be then extracted (at  $0^+$  ps) from the graphic representation given in Figure 6 and then, it is found  $\zeta \approx 400$  nm for a 800 nm pump laser irradiation, as physically expected.

If the simulation of the deformation field  $\eta$  remains of a strong interest, the simulation of the  $\frac{\Delta R}{R}$  quantity is also important, as this parameter is experimentally measured.

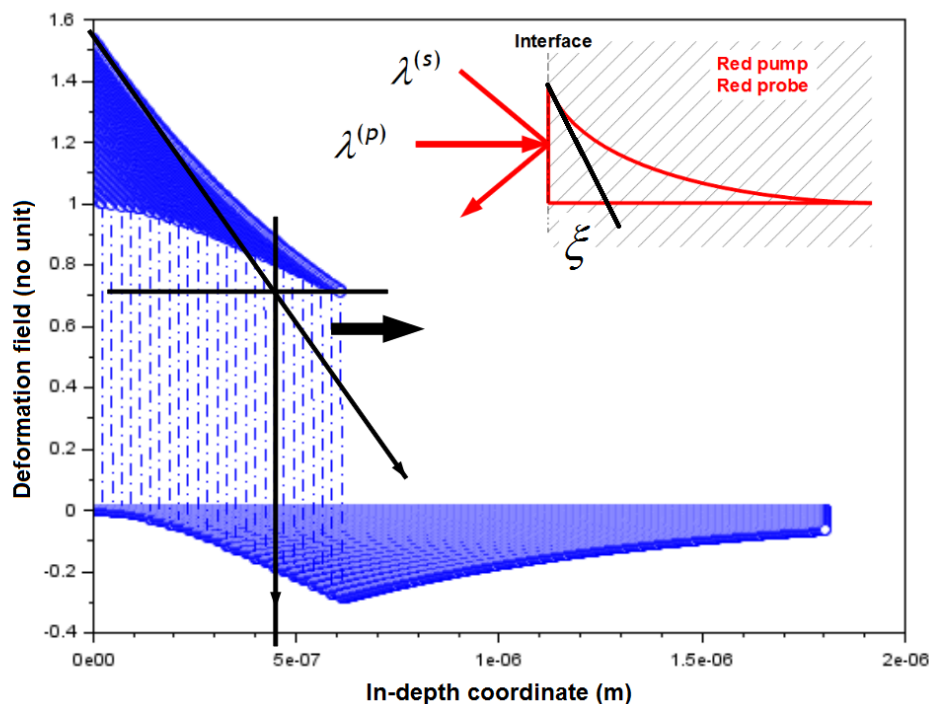


**Figure 6.** Numerical results concerning the spatial evolution of the deformation field (in-depth coordinate). All parameters given into the code lines. Insert: red-red beams interacting with the medium. Estimation of the optical depth penetration  $\zeta \approx 450$  nm, using the graphic representation (black lines added onto the simulation). Experimental conditions for the simulation: field simulation considered at 0 nm (interface), 1.55 eV deposited energy corresponding to a 800.8 nm wavelength, angle of incidence of the laser beams  $45^\circ$ , set-up described in Figure 2.

```

//Scilab code (part 09/13)
//Photo-induced deformation field (red pump beam)

//Coefficient Ra20
Ra20=(-ZGaAs+Z0)/(ZGaAs+Z0)

scf(0)
clf(0)

//Time between 0 ps and 100 ps, step of 1ps
for t=0:5e-12:130e-12;
//initial index p
p=0;

//Space variable from 0.5 nm to 800 nm (bulk), step of 1 nm
for z=0e-9:2.5e-9:1800e-9;
p=p+1;

//Direct propagation of the wavefront into the bulk
defs3(p)=
(2-exp(-alphan.*VLGaAsEstim.*t))*exp(-alphan*z)*H(z)-
H((z)-VLGaAsEstim*t)*exp(-alphan*abs((z)-VLGaAsEstim*t));
//defor3(p)= H(z-VLGAAsEstim*t)*exp(-alphan*abs(z-VLGAAsEstim*t));
defs(p)=1*defs3(p);

end
z=0e-9:2.5e-9:1800e-9;
plot(z,defs,'-.o')
xlabel('In-depth direction (m)')
ylabel('Deformation field (no unit)')
title('Spatial evolution of the deformation
field for in-depth coordinate. Interface air/GaAs at 0 nm')
end

```

## 2.6. Transient Optical Reflectivity Simulation

During the experiments, the coherent acoustic phonons are photo-detected temporally monitoring the ultrafast transient changes of the detected optical reflectivity  $\frac{\Delta R}{R}(\lambda, t)$  [8], using the common optical architecture similar to the one given in Figure 2 [4,8,46]. The pump can be considered as a trigger inducing all the dynamics into the matter, under a conversion process of the optical energy of the pump beam into mechanical energy (Figure 1). The reflected laser beam (probe) intensity changes are collected by a photodiode, under the saturation laser intensity threshold. Into these typical reflectometry measurements [13], the first incident optical pulse (pump) is then absorbed beneath the substrate surface [4]. The photocreated dilatation generates a strain pulse typically within the optical depth penetration  $\zeta$ . As the optical properties of the substrate are modified under strain (through a variation of refractive index  $\Delta \tilde{n}$  or of the dielectric constant  $\Delta \tilde{\epsilon}$ , as given in Figure 1), the probe pulse allows to get the phase  $\phi$  and the amplitude  $A$  of the acoustic signal (through a photo-elastic coupling, as described in Figure 1). The acousto-optic interaction is found wavelength dependent [10,47,48].

The existence of acoustic waves or acoustic disturbances into the bulk of the material modifies the transient reflectivity  $\frac{\Delta R}{R}(t)$ , which is the physical key-quantity for monitoring acoustic wave propagating inside the medium. Either motions of the crystal surface [49–51] and bulk acoustic

propagation phenomena [52–54] can be optically detected using this ultrasonic approach (Figure 1). All the simulations given into the present work are conducted considering the experimental set-up given in Figure 2 and into the conditions previously given in the text.

Photo-elastic coefficients ( $p_{11}$  and  $p_{12}$ ) [55] of the elastic tensor  $p_{ij}$  and stiffness coefficients  $C_{11}$  and  $C_{12}$  of the reduced elastic tensor  $C_{mn}$  are used to define the total photo-elastic coefficient  $pe_{GaAs}$ :

$$pe_{GaAs} = \frac{1}{2n_{GaAs}^{(s)}} \times \frac{2\pi}{\lambda^{(s)}} \times (p_{11}C_{11} + 2p_{12}C_{12}) \quad (13)$$

in which  $\lambda^{(s)}$  corresponds to the optical probe wavelength. The numerical result (for 800.8 nm) is  $pe_{GaAs} = 41.2853 + 33.5125i$ , and can be reintroduced into the simulation codes afterwards. This expression can also be described under the following derivative expression:

$$pe_{GaAs} = \frac{\partial k_{GaAs}}{\partial \eta} = \frac{2\pi}{\lambda^{(s)}} \times \frac{\partial n_{GaAs}}{\partial \eta} \equiv \frac{2\pi}{\lambda^{(s)}} \times pe \quad (14)$$

introducing the quantity  $pe$  and the optical wavenumber  $k_{GaAs}^{(s)}$  of the probe laser beam defined by:

$$pe = \frac{\partial n_{GaAs}}{\partial \eta} = \frac{p_{11}C_{11} + 2p_{12}C_{12}}{2n_{GaAs}^{(s)}} \quad (15)$$

considering:

$$k_{GaAs}^{(s)} = \frac{2\pi}{\lambda^{(s)}} \times n_{GaAs}^{(s)} \quad (16)$$

Schematically, the presence of the mechanical stress into the matter generates a birefringence effect. The larger the photoelastic constant is, the stronger the birefringence signal generated by the mechanical stress. The photo-elastic coefficients ( $p_{11}$ ,  $p_{12}$  and  $p_{44}$ ) depend on the crystal nature of the material and on the optical wavelength considered [56].

```
//Scilab code (part 10/13)
p11=(8+%i*(3))*1e-9; //Coefficient at 800 nm
p12=(-4+%i*(-3))*1e-9; //Coefficient at 800 nm

pe=(p11*c11+2*p12*c12)/(2*n2s)

//Photo-elastic coefficient (p11, p12, p44) of the photo-elastic tensor
pe2=1*(2*%pi/lambdas)*(p11*c11+2*p12*c12)/(2*n2s)

//to compare with (test):
//Photo-elastic coefficient (p11, p12, p44) of the photo-elastic tensor
pe2=1*(2*%pi/lambdas)*pe
```

Considering a single interface (air-substrate), the transient complex reflectivity [7] is given by:

$$\frac{\Delta r}{r_{01}} = 2ik_0u(0) + i \frac{(1 - r_{02}^2)}{r_{02}} \times \frac{\partial \tilde{k}_{GaAs}}{\partial \eta} \times \int_0^{+\infty} \eta(z, t) \times e^{2ik_{GaAs}z} dz \quad (17)$$

in which  $r_{02}$  corresponds to the optical reflexion coefficient at the  $z = 0$  interface [7] (air-substrate interface). In this expression, two contributions can be distinguished: an interface effect and a bulk effect (including a *Laplace* transform of the deformation field  $\eta$ ). The interface corresponds to a mechanically free single surface.  $u(0)$  corresponds to the displacement of the front surface.

The probe light absorption in the surrounding air is supposed negligible during air propagation. The acousto-optical information is contained in the previously given photo-elastic coefficient expression (detection process):

$$\frac{\partial \tilde{k}_{GaAs}}{\partial \eta} = \frac{\partial k'_{GaAs}}{\partial \eta} + i \frac{\partial k''_{GaAs}}{\partial \eta} \quad (18)$$

in accordance with the following optical complex wavevector expression:

$$\tilde{k}_{GaAs} = k'_{GaAs} + ik''_{GaAs} \quad (19)$$

The transient complex optical reflectivity is linked to the real optical transient reflectivity by the relation  $R = rr^*$ , if  $r^*$  corresponds to the conjugated complex of  $r$  [1,54], and, therefore, the amplitude  $A(t)$ , which corresponds to the measured quantity, is given by:

$$\frac{A}{2}(t) \cong \frac{\Delta R}{2R_0}(t) = \Re \left\{ \frac{\Delta r}{r_0}(t) \right\} \quad (20)$$

The phase variation  $\Delta\phi$  could also be extracted, considering the imaginary part of the complex transient reflectivity:

$$\Delta\phi = \Im \left( \frac{\Delta r}{r_0} \right) \quad (21)$$

This phase variation will not be considered for the present study, as the optically measured physical quantity is the reflectivity  $\frac{\Delta R}{R_0}(t)$ . From the analysis of the Brillouin oscillations (oscillating component) present into the reflectivity signal measured, all the spectral modes (frequency domain) [7,53,57,58] can be afterwards extracted, and informations onto the material itself (microcracks, velocities, attenuation, or charge carriers phenomena) can be evaluated. The initial peak (zero-time peak, and 0–5 ps temporal range) corresponds to pure electronic phenomenon and it will not be modelised into the present work, as it focuses only onto purely acoustic wave propagation phenomenon (temporal established phenomenon).

A thermal decreasing background can be superimposed to the pure transient reflectometric signal modelized, to simulate the exponential decay related to the pure thermal phenomenon. It is chosen a simple exponential decay  $A \times \exp\left(-\frac{t}{\tau}\right)$ .  $A$  corresponds to an arbitrary scale factor (constant), and it seems to be physically acceptable to choose  $\tau \approx 20$  ps, as this value permits a relevant and good fit of real experimental case.

A FFT (*Fast Fourier Transform*) permits to identify the vibration modes photo-induced by the optical pump. Sampling conditions are specifically chosen (sample rate, number of samples) to match the *Nyquist-Shannon* criteria [59].

```
//Scilab code (part 11/13)
k2s=2*pi*n2s/lambdas //n2s related to the probe into GaAs

r02=(n2s-n0)/(n0+n2s) //Reflexion coefficient
//Acoustic interface air-GaAs (at normal incidence)

//Factor F for deformation integration
F=(1-r02*r02)/r02

//Coefficient Ra20 (impedance ZGaAs and Z0 for air)
Ra20=(-ZGaAs+Z0)/(ZGaAs+Z0)
```

```

//Scilab code (part 12/13)
//Transient reflectivity (integration of deformation field)
intS=0;
//defor1=0;
//defor2=0;
defor3=0;
k=0;
for t=0:1e-12:6000e-12; //from 0 to 6 ns (time domain)
k=k+1;

r=0;
for z=0:1e-9:1800e-9; //from 0 to 1800 nm (space domain)
r=r+1;
defor3(r)=(defo(alphap,t,z).*exp(2*%i*k2s*z))';
end
z=0:1e-9:1800e-9; //from 0 to 1800 nm (space domain for integration)
intS(k)=0.5*pe2*(1/r02-r02).*inttrap(z,defor3); //Trapezoidal integration
end

t=0:1e-12:6000e-12; //from 0 to 6 ns (time domain)
//Transient reflectivity variation (empiric exponential decay added)
drr=real(intS')+50*exp(-t/(20e-12));

scf(1)
clf(1)

plot2d(t,drr); //Simulation graphic representation

```

```

//Scilab code (part 13/13)
sample_rate=1e12
t = 0e-12:1/sample_rate:6000e-12
N=size(t,'*') //number of samples

g=fft(drr,-1)

f=sample_rate*(0:(N/2))/N; //associated frequency vector
n=size(f,'*')

scf(2) //clear the figure
clf(2)

//Maximum values for frequencies
[m,k]=max(f)
answer=max(f) //maximum vertical axis (m)

plot(f,abs(g(1:n)));

```

The numerical results obtained from the simulation are in strong accordance with experimental dataset (Figure 7), considering the experimental set-up described in Figure 2. A good correlation is

found concerning *FFT* spectral components (Figure 8). Possible slight frequency shifts can be due to experimental uncertainty related to the value of the angle of incidence  $\theta$  (experimental set-up), as this parameter could impact the Brillouin signal.

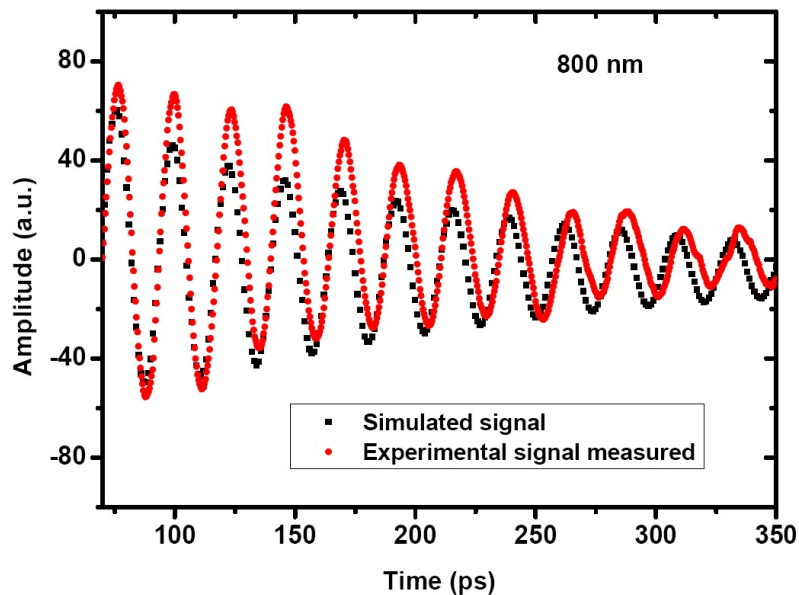


**Figure 7.** Numerical results concerning the reflectivity intensity signal and the related FFT data (insert), obtained using the experimental set-up given in Figure 2. Comparison of experimental and simulated (each at 800 nm for laser beams) signals between 70 ps and 350 ps.

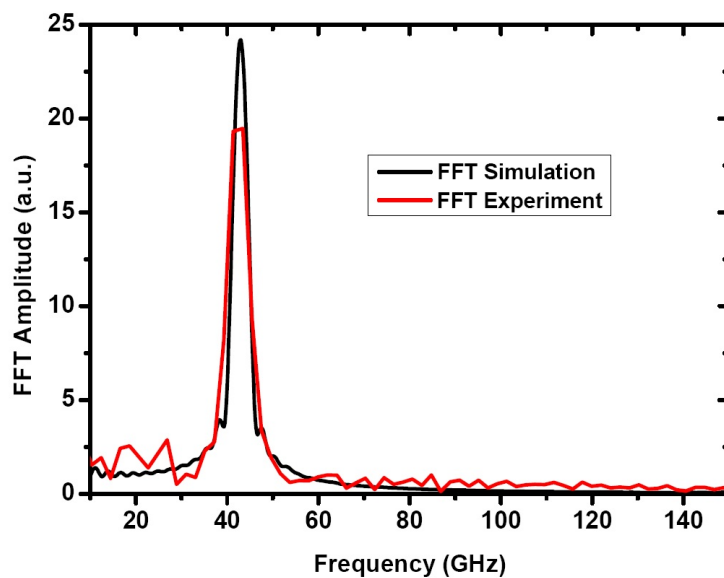


**Figure 8.** Numerical results concerning the related FFT amplitude, good accordance between experimental measured data and simulation. Hanning window.

### 3. Conclusions

A complete numerical toolbox concerning photo-induced propagative acoustic wavefronts and laser ultrasonics is proposed, providing step-by-step codes. Few orders of magnitudes are calculated, such as acoustic pulse duration, acoustic typical frequency, optical absorption coefficient, and optical depth penetration. Acoustic velocities have been numerically evaluated, taking into account angular

laser beam incidence dependence and temperature impact. Brillouin frequencies have been evaluated for LA, TA, QLA and QTA acoustical modes into a commonly used red pump–red-probe configuration. A deformation field simulation is given. The complex transient reflectivity is numerically described. The reflectivity signal with/without an empiric superimposed background thermal decay is also given. Numerical calculations of FFT give the opportunity to extract the mode of vibration in GHz, which can be easily compared to experimentally measured datasheets (under good matching).

**Funding:** This research was funded by ANR grant number ANR-06-BLAN-0013. The founding sponsors had no role into the design of the study; in the collection, analyses, or interpretation of data; in the writing of the manuscript, and in the decision to publish the result.

**Acknowledgments:** Experimental works were all performed in Condensed State Physics Laboratory (LPEC/CNRS), 72085 Le Mans Cedex 09, France. The author would like to thank Pascal Ruello (CNRS I3M, France), Vitali Gusev (CNRS LAUM, France), Ayman Al Falou from IEEE/OSA for scientific discussions, and C. Thomas from Rennes 1 university (France) for advice.

**Conflicts of Interest:** The author declares no conflict of interest.

## References

1. Thomsen, C.; Strait, J.; Vardeny, Z.; Maris, H.J.; Tauc, J.; Hauser, J. Coherent phonon generation and detection by picosecond light pulses. *Phys. Rev. Lett.* **1984**, *53*, 989. [[CrossRef](#)]
2. Eesley, G.L.; Clemens, B.M.; Paddock, C.A. Generation and detection of picosecond acoustic pulses in thin metal films. *Appl. Phys. Lett.* **1987**, *50*, 717–719. [[CrossRef](#)]
3. Ruello, P.; Gusev, V.E. Physical mechanisms of coherent acoustic phonons generation by ultrafast laser action. *Ultrasonics* **2015**, *56*, 21–35. [[CrossRef](#)]
4. Gusev, V. Laser hypersonics in fundamental and applied research. *Acustica* **1996**, *82*, S-37–S-45.
5. Kozhushko, V.V.; Hess, P. Laser-induced focused ultrasound for nondestructive testing and evaluation. *J. Appl. Phys.* **2008**, *103*, 124902. [[CrossRef](#)]
6. Ivochkin, A.Y.; Karabutov, A.; Lyamshev, M.; Pelivanov, I.; Rohatgi, U.; Subudhi, M. Measurement of velocity distribution for longitudinal acoustic waves in welds by a laser optoacoustic technique. *Acoust. Phys.* **2007**, *53*, 471–477. [[CrossRef](#)]
7. Thomsen, C.; Grahn, H.T.; Maris, H.J.; Tauc, J. Surface generation and detection of phonons by picosecond light pulses. *Phys. Rev. B* **1986**, *34*, 4129. [[CrossRef](#)]
8. Babilotte, P.; Ruello, P.; Mounier, D.; Pezeril, T.; Vaudel, G.; Edely, M.; Breteau, J.; Gusev, V.; Blary, K. Femtosecond laser generation and detection of high-frequency acoustic phonons in GaAs semiconductors. *Phys. Rev. B* **2010**, *81*, 245207. [[CrossRef](#)]
9. Devos, A.; Cote, R.; Caruyer, G.; Lefevre, A. A different way of performing picosecond ultrasonic measurements in thin transparent films based on laser-wavelength effects. *Appl. Phys. Lett.* **2005**, *86*, 211903. [[CrossRef](#)]
10. Devos, A.; Lerouge, C. Evidence of laser-wavelength effect in picosecond ultrasonics: Possible connection with interband transitions. *Phys. Rev. Lett.* **2001**, *86*, 2669. [[CrossRef](#)]
11. Perrin, B.; Bonello, B.; Jeannet, J.; Romatet, E. Interferometric detection of hypersound waves in modulated structures. *Prog. Nat. Sci.* **1996**, *6*, S444–S448.
12. Wiesenfeld, J.M. Acoustic phonon generation in the picosecond dynamics of dense electron-hole plasmas in InGaAsP films. *Appl. Phys. Lett.* **1985**, *47*, 143–145. [[CrossRef](#)]
13. Thomsen, C.; Grahn, H.; Maris, H.; Tauc, J. Picosecond interferometric technique for study of phonons in the Brillouin frequency range. *Opt. Commun.* **1986**, *60*, 55–58. [[CrossRef](#)]
14. Gusev, V.E.; Karabutov, A.A. Laser Optoacoustics. In *NASA STI/Recon Technical Report A*; NASA: Washington, DC, USA, 1991; Volume 93.
15. Grahn, H.T.; Maris, H.J.; Tauc, J. Picosecond ultrasonics. *IEEE J. Quantum Electron.* **1989**, *25*, 2562–2569. [[CrossRef](#)]
16. Karabutov, A.; Larichev, V.; Maksimov, G.; Pelivanov, I.; Podymova, N. Relaxation dynamics of a broadband nanosecond acoustic pulse in a bubbly medium. *Acoust. Phys.* **2006**, *52*, 582–588. [[CrossRef](#)]
17. Shelton, L.; Yang, F.; Ford, W.; Maris, H. Picosecond ultrasonic measurement of the velocity of phonons in water. *Phys. Status Solidi B* **2005**, *242*, 1379–1382. [[CrossRef](#)]

18. Tas, G.; Stoner, R.; Maris, H.; Rubloff, G.; Oehrlein, G.; Halbout, J. Noninvasive picosecond ultrasonic detection of ultrathin interfacial layers: CF x at the Al/Si interface. *Appl. Phys. Lett.* **1992**, *61*, 1787–1789. [[CrossRef](#)]
19. Lomonosov, A.; Mayer, A.P.; Hess, P. 3. Laser-based surface acoustic waves in materials science. *Exp. Methods Phys. Sci.* **2001**, *39*, 65–134.
20. Bennis, A.; Lomonosov, A.; Shen, Z.; Hess, P. Laser-based measurement of elastic and mechanical properties of layered polycrystalline silicon structures with projection masks. *Appl. Phys. Lett.* **2006**, *88*, 101915. [[CrossRef](#)]
21. Lehmann, G.; Lomonosov, A.; Hess, P.; Gumbsch, P. Impulsive fracture of fused quartz and silicon crystals by nonlinear surface acoustic waves. *J. Appl. Phys.* **2003**, *94*, 2907–2914. [[CrossRef](#)]
22. Kozhushko, V.V.; Hess, P. Anisotropy of the strength of Si studied by a laser-based contact-free method. *Phys. Rev. B* **2007**, *76*, 144105. [[CrossRef](#)]
23. Dubois, M.; Drake, T.E., Jr. Evolution of industrial laser-ultrasonic systems for the inspection of composites. *Nondestruct. Test. Eval.* **2011**, *26*, 213–228. [[CrossRef](#)]
24. Dubois, M.; Burr, K.C.; Drake, T.E. Laser phase noise reduction for industrial interferometric applications. *Appl. Opt.* **2004**, *43*, 4399–4407. [[CrossRef](#)] [[PubMed](#)]
25. Karabutov, A.; Devichensky, A.; Ivochkin, A.; Lyamshev, M.; Pelivanov, I.; Rohadgi, U.; Solomatin, V.; Subudhi, M. Laser ultrasonic diagnostics of residual stress. *Ultrasonics* **2008**, *48*, 631–635. [[CrossRef](#)] [[PubMed](#)]
26. Xu, M.; Wang, L.V. Photoacoustic imaging in biomedicine. *Rev. Sci. Instrum.* **2006**, *77*, 041101. [[CrossRef](#)]
27. Miklós, A.; Pei, S.C.; Kung, A. Multipass acoustically open photoacoustic detector for trace gas measurements. *Appl. Opt.* **2006**, *45*, 2529–2534. [[CrossRef](#)]
28. Miklós, A.; Hess, P.; Bozóki, Z. Application of acoustic resonators in photoacoustic trace gas analysis and metrology. *Rev. Sci. Instrum.* **2001**, *72*, 1937–1955. [[CrossRef](#)]
29. Bonello, B.; Armand, F.; Pradeau, J.; Perez, H.; Perrin, B.; Louis, G. Evidence for the alteration of an organic/metal interface resulting from the formation of a broad interfacial layer. *J. Appl. Phys.* **1999**, *86*, 4959–4963. [[CrossRef](#)]
30. Moura, A.; Lomonosov, A.M.; Hess, P. Depth evaluation of surface-breaking cracks using laser-generated transmitted Rayleigh waves. *J. Appl. Phys.* **2008**, *103*, 084911. [[CrossRef](#)]
31. Jian, X.; Dixon, S.; Guo, N.; Edwards, R. Rayleigh wave interaction with surface-breaking cracks. *J. Appl. Phys.* **2007**, *101*, 064906. [[CrossRef](#)]
32. Kim, H.; Jhang, K.; Shin, M.; Kim, J. A noncontact NDE method using a laser generated focused-Lamb wave with enhanced defect-detection ability and spatial resolution. *Ndt E Int.* **2006**, *39*, 312–319. [[CrossRef](#)]
33. Weiss, E.C.; Lemor, R.M.; Pilarczyk, G.; Anastasiadis, P.; Zinin, P.V. Imaging of focal contacts of chicken heart muscle cells by high-frequency acoustic microscopy. *Ultrasound Med. Biol.* **2007**, *33*, 1320–1326. [[CrossRef](#)] [[PubMed](#)]
34. Monchalain, J.P. Laser-Ultrasonics: From the Laboratory to Industry. *AIP Conf. Proc.* **2004**, *700*, 3–31.
35. Delale, C. *Bubble Dynamics and Shock Waves*; Springer: Berlin/Heidelberg, Germany, 2012.
36. Castro, A.P.; Alves, H.W.L. Kinetic Monte Carlo simulation of the nitridation of the GaAs (100) surfaces. *Braz. J. Phys.* **2006**, *36*, 305–308. [[CrossRef](#)]
37. Biegelsen, D.K.; Bringans, R.D.; Northrup, J.E.; Swartz, L.E. Surface reconstructions of GaAs(100) observed by scanning tunneling microscopy. *Phys. Rev. B* **1990**, *41*, 5701–5706. [[CrossRef](#)]
38. Lu, Z.H.; Lagarde, C.; Sacher, E.; Currie, J.F.; Yelon, A. A surface analytical study of GaAs(100) cleaning procedures. *J. Vacuum Sci. Technol. A* **1989**, *7*, 646–650. [[CrossRef](#)]
39. Blakemore, J.S. Semiconducting and other major properties of gallium arsenide. *J. Appl. Phys.* **1982**, *53*, R123–R181. [[CrossRef](#)]
40. Wright, O.; Perrin, B.; Matsuda, O.; Gusev, V. Ultrafast carrier diffusion in gallium arsenide probed with picosecond acoustic pulses. *Phys. Rev. B* **2001**, *64*, 081202. [[CrossRef](#)]
41. Devos, A.; Robillard, J.F.; Côte, R.; Emery, P. High-laser-wavelength sensitivity of the picosecond ultrasonic response in transparent thin films. *Phys. Rev. B* **2006**, *74*, 064114. [[CrossRef](#)]
42. Burenkov, Y.A.; Burdukov, Y.M.; Davydov, S.Y.; SP, N. Temperature-dependence of gallium-arsenide elastic-constants. *Fiz. Tverd. Tela* **1973**, *15*, 1757–1761.

43. Cote, R.; Devos, A. Refractive index, sound velocity and thickness of thin transparent films from multiple angles picosecond ultrasonics. *Rev. Sci. Instrum.* **2005**, *76*, 053906. [[CrossRef](#)]
44. Mechri, C.; Ruello, P.; Gusev, V. Confined coherent acoustic modes in a tubular nanoporous alumina film probed by picosecond acoustics methods. *New J. Phys.* **2012**, *14*, 023048. [[CrossRef](#)]
45. Wright, O. Thickness and sound velocity measurement in thin transparent films with laser picosecond acoustics. *J. Appl. Phys.* **1992**, *71*, 1617–1629. [[CrossRef](#)]
46. Akhmanov, S.A.; Gusev, V.É. Laser excitation of ultrashort acoustic pulses: New possibilities in solid-state spectroscopy, diagnostics of fast processes, and nonlinear acoustics. *Physics-Uspokhi* **1992**, *35*, 153–191. [[CrossRef](#)]
47. Devos, A.; Le Louarn, A. Strong effect of interband transitions in the picosecond ultrasonics response of metallic thin films. *Phys. Rev. B* **2003**, *68*, 045405. [[CrossRef](#)]
48. Devos, A.; Côte, R. Strong oscillations detected by picosecond ultrasonics in silicon: Evidence for an electronic-structure effect. *Phys. Rev. B* **2004**, *70*, 125208. [[CrossRef](#)]
49. Rothenberg, J.E. Observation of the transient expansion of heated surfaces by picosecond photothermal deflection spectroscopy. *Opt. Lett.* **1988**, *13*, 713–715. [[CrossRef](#)] [[PubMed](#)]
50. Wright, O.; Gusev, V. Acoustic generation in crystalline silicon with femtosecond optical pulses. *Appl. Phys. Lett.* **1995**, *66*, 1190–1192. [[CrossRef](#)]
51. Wright, O.B.; Gusev, V.E. Ultrafast generation of acoustic waves in copper. *IEEE Trans. Ultrason. Ferroelectr. Freq. Control* **1995**, *42*, 331–338. [[CrossRef](#)]
52. Wright, O.B.; Hyoguchi, T.; Kawashima, K. Laser picosecond acoustics in thin films: Effect of elastic boundary conditions on pulse generation. *Japan. J. Appl. Phys.* **1991**, *30*, L131. [[CrossRef](#)]
53. Wright, O.B.; Kawashima, K. Coherent phonon detection from ultrafast surface vibrations. *Phys. Rev. Lett.* **1992**, *69*, 1668. [[CrossRef](#)] [[PubMed](#)]
54. Wright, O.; Gusev, V. Ultrafast acoustic phonon generation in gold. *Physica B* **1996**, *219*, 770–772. [[CrossRef](#)]
55. Nelson, D.; Lax, M. New symmetry for acousto-optic scattering. *Phys. Rev. Lett.* **1970**, *24*, 379. [[CrossRef](#)]
56. Etchegoin, P.; Kircher, J.; Cardona, M.; Grein, C.; Bustarret, E. Piezo-optics of GaAs. *Phys. Rev. B* **1992**, *46*, 15139. [[CrossRef](#)]
57. Lin, H.; Maris, H.J.; Freund, L.B.; Lee, K.Y.; Luhn, H.; Kern, D.P. Study of vibrational modes of gold nanostructures by picosecond ultrasonics. *J. Appl. Phys.* **1993**, *73*, 37–45. [[CrossRef](#)]
58. Chen, W.; Maris, H.J.; Wasilewski, Z.R.; Tamura, S.I. Attenuation and velocity of 56 GHz longitudinal phonons in gallium arsenide from 50 to 300 K. *Philos. Mag. B* **1994**, *70*, 687–698. [[CrossRef](#)]
59. Jerri, A.J. The Shannon sampling theorem—Its various extensions and applications: A tutorial review. *Proc. IEEE* **1977**, *65*, 1565–1596. [[CrossRef](#)]

